Revisiting the Stellar Mass–Angular Momentum–Morphology Relation: Extension to Higher Bulge Fraction and the Effect of Bulge Type

Sarah M. Sweet[1] , David Fisher[1], Karl Glazebrook[1] , Danail Obreschkow[2] , Claudia Lagos[2] , and Liang Wang[2]

[1] Centre for Astrophysics and Supercomputing, Swinburne University of Technology, PO Box 218, Hawthorn VIC 3122, Australia; sarah@sarahsweet.com.au

[2] International Centre for Radio Astronomy Research, University of Western Australia, 7 Fairway, Crawley, WA 6009, Australia

Abstract

We present the relation between stellar specific angular momentum j_*, stellar mass M_*, and bulge-to-total light ratio β for The H I Nearby Galaxy Survey, the Calar Alto Legacy Integral Field Area Survey, and Romanowsky & Fall data sets, exploring the existence of a fundamental plane between these parameters, as first suggested by Obreschkow & Glazebrook. Our best-fit M_*–j_* relation yields a slope of $\alpha = 1.03 \pm 0.11$ with a trivariate fit including β. When ignoring the effect of β, the exponent $\alpha = 0.56 \pm 0.06$ is consistent with $\alpha = 2/3$ that is predicted for dark matter halos. There is a linear β–j_*/M_* relation for $\beta \lesssim 0.4$, exhibiting a general trend of increasing β with decreasing j_*/M_*. Galaxies with $\beta \gtrsim 0.4$ have higher j_* than predicted by the relation. Pseudobulge galaxies have preferentially lower β for a given j_*/M_* than galaxies that contain classical bulges. Pseudobulge galaxies follow a well-defined track in β–j_*/M_* space, consistent with Obreschkow & Glazebrook, while galaxies with classical bulges do not. These results are consistent with the hypothesis that while growth in either bulge type is linked to a decrease in j_*/M_*, the mechanisms that build pseudobulges seem to be less efficient at increasing bulge mass per decrease in specific angular momentum than those that build classical bulges.

Key words: galaxies: bulges – galaxies: elliptical and lenticular, cD – galaxies: evolution – galaxies: fundamental parameters – galaxies: kinematics and dynamics – galaxies: spiral

Supporting material: machine-readable table

1. Introduction

Galaxy stellar mass M_* and angular momentum J are fundamental properties of galaxies; they have been shown to correlate strongly with galaxy size and density (Mo et al. 1998), disk thickness and color (Hernandez & Cervantes-Sodi 2006), and morphology (Romanowsky & Fall 2012; Obreschkow & Glazebrook 2014; Cortese et al. 2016, hereafter RF12, OG14, and C16, respectively).

M and J are not independent in that J is scaled by mass, so the standard method for studying their relationship is to remove the mass dependence to obtain specific angular momentum $j = J/M$. Specific angular momentum of baryons in the galaxy $j_{\rm baryons}$ is empirically similar to that of the dark matter halo j_h (Fall 1983). This similarity is expected for baryons in the halo, since the same tidal forces are experienced during spin-up (Barnes & Efstathiou 1987; Catelan & Theuns 1996a, 1996b; van den Bosch et al. 2001), but has been historically difficult to reconcile for baryons in the disk, viz. the "angular momentum catastrophe" (Governato et al. 2010; Agertz et al. 2011). $j_{\rm baryons}$ is typically further resolved into analogous specific angular momenta for stars, Hα, H I, and H$_2$ (j_*, $j_{\rm H\alpha}$, $j_{\rm H\,I}$, and $j_{\rm H_2}$, respectively) depending on the observed kinematics and mass profiles[3] available to be studied. In this work we focus on stellar specific angular momentum $j_* = J_*/M_*$.

The observational M_*–j_* plane was first studied by Fall (1983), who found $j_* \propto q M_*^\alpha$, with parallel tracks defined by late-type and early-type galaxies. These tracks have exponent $\alpha = 2/3$, which is in agreement with the natural scaling of cold dark matter (CDM) halos in a hierarchical universe. RF12 later studied the relation between M_*, j_*, and β, confirming the

earlier result of $j \propto M_*^{2/3}$, with a factor of q depending on whether disks or bulges are considered. OG14 used high-quality observations of 16 galaxies from The H I Nearby Galaxy Survey (THINGS, Leroy et al. 2008; Walter et al. 2008) to further investigate the M_*–j_*–β relation and found that $\alpha = 2/3$ for $0 \leqslant \beta \leqslant 0.32$, but that $\alpha \sim 1$ when β is treated as a free parameter. More recently, C16 analyzed a subset of galaxies from the Sydney-AAO Multi-object Integral field (SAMI, Croom et al. 2012) Galaxy Survey (Allen et al. 2015; Bryant et al. 2015; Sharp et al. 2015) and similarly found, when considering j at one effective radius r_e, that α is consistent with $2/3$ for the whole range of morphologies, but is higher when a single morphology class is considered and approaches $\alpha = 1$ for late-type galaxies.

There is a known dichotomy in the properties of pseudo- versus classical bulges (e.g., Kormendy & Kennicutt 2004; Fisher & Drory 2016); classical bulges are pressure-supported components thought to be formed by minor mergers (Toomre 1977; Schweizer 1990) or disk instabilities (Toomre 1964), while pseudobulges are rotationally supported components formed during the secular evolution of the disk, so they naturally have higher j_* (Wyse et al. 1997; Kormendy & Kennicutt 2004). Classical bulges generally contribute larger β than pseudo- bulges (Fisher & Drory 2016). These properties are intimately related to galaxy angular momentum and morphology. However, previous studies of the M_*–j_*–β relation have not analyzed galaxies that contain classical bulges separately from those that contain pseudobulges, so the effect of the bulge type is unknown.

In this work we investigate the effect of bulge type on the relationship between stellar mass, specific angular momentum, and morphology across a large range of β, by combining OG14 with high-quality subsets of the sample in RF12 and in the

---

[3] Surface density is typically used as a proxy; j does not have the mass scaling of J, but the mass profile is used as a weighting factor.
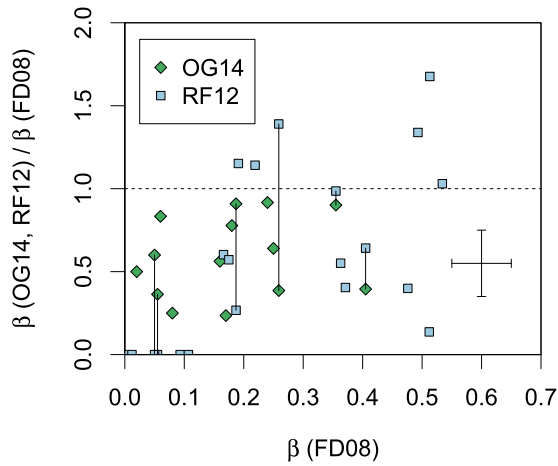
Figure 1. Comparison between bulge-to-total ratio β methods. THINGS galaxies presented in OG14 are shown as green filled diamonds; galaxies in RF12 as blue filled squares. Galaxies appearing in both RF12 and OG14 are joined with solid lines. The dashed line represents the 1:1 relation. A typical error bar is shown. Both RF12 and OG14 methods tend to underestimate β with respect to our method that was described in Fisher & Drory (2008).

Calar Alto Legacy Integral Field Area Survey (CALIFA, Sánchez et al. 2012, 2016; Husemann et al. 2013; Walcher et al. 2014). In Section 2 we describe our methods for measuring bulge properties and j_*, and introduce the data sets. In Section 3 we present the M_*–j_*–β relation as it relates to bulge type, given the known dichotomy in the properties of pseudo- versus classical bulges and the galaxies that host them (e.g., Kormendy & Kennicutt 2004; Fisher & Drory 2016). Section 4 concludes this paper with a discussion of the significance of these results.

2. Sample and Methods

We combine observations from THINGS, RF12, and CALIFA data sets to trace the fundamental relation between M_*, j_*, and β over a wide range of β. The three samples are complementary. We have high-quality j_*, β, and bulge classifications for THINGS, but the sample is limited to low to moderate β, with few galaxies that contain classical bulges. We thus employ the RF12 galaxies, for which we have high-quality β and bulge classification to extend our sample to higher β and increase the number of galaxies with classical bulges. Similarly, we also include a subset of the CALIFA sample, for which we measure high-quality j_* and a greater range of β. Below we present our methods for determining bulge properties and j_* before giving specific details for each of our samples.

2.1. Bulge-to-total Mass Ratio and Type

We obtain bulge properties by cross-correlating the OG14 and RF12 samples with the combined data set of Fisher & Drory (2010, 2011), Fabricius et al. (2012), and Fisher et al. (2013). These samples use the same method, software, and wavelength range to conduct 2D bulge–disk decompositions (described in Fisher & Drory 2008, FD08). The method combines high-resolution *Hubble Space Telescope* (*HST*) imaging with wide-field ground-based imaging to reduce uncertainties and degeneracies inherent to bulge–disk decompositions. It also accounts for the different mass-to-light ratio of the bulge and disk. Conversely, OG14 simply measured the

bulge as the excess light over a fitted exponential disk, while RF12 fitted two elliptical isophotes in projection (Kent 1986). Figure 1 compares FD08's β with OG14 and RF12, illustrating that OG14 and RF12 present β that are mutually inconsistent and systematically underestimated with respect to FD08. Importantly, our consistent method allows for an accurate comparison of bulge properties between OG14 and RF12, with an uncertainty of $\Delta\beta_{\text{FD08}} = \pm 0.05$.

We use the well-known correlation between the bulge Sérsic index, n_b (Sérsic 1963), and the bulge type (Fisher & Drory 2008, 2016) to classify galaxies that contain pseudo-bulges and classical bulges, such that $n_b < 2$ implies a galaxy with a pseudobulge, and $n_b > 2$ implies a galaxy with a classical bulge. The exception is NGC 3593 in RF12, with a low $n_b \approx 1.2$, which would ordinarily imply that it contains a pseudobulge. However, its bulge is "not classifiable" (Fabricius et al. 2012) for the following reasons: (1) NGC 3593 is an extreme example of counter-rotating kinematics (Bertola et al. 1996; Fabricius et al. 2012), suggesting a recent merger (e.g., Bassett et al. 2017), and the empirical methods of bulge classification fail for most galaxies that are experiencing interactions (Fisher & Drory 2016); (2) the surface photometry cannot be reliably fit due to the chaotic dust profile (Ravindranath et al. 2001); and (3) the galaxy has a "peculiar" global morphology (e.g., Sandage & Bedke 1994).

2.2. Specific Angular Momentum

We adopt the same method as Obreschkow et al. (2015) for calculating j_* from integral field spectroscopic (IFS) observations. Compared with the slit spectroscopy, this method significantly increases accuracy in tracing the kinematic field, since kinematic and photometric major axes may be misaligned (e.g., Sweet et al. 2016), and the velocity fields of many galaxies are not well described by simple 1D rotation curves.

We use a combination of the observed, deprojected angular momentum where available, together with a model-informed estimate of the deprojected angular momentum in the spaxels where observations are not of sufficient quality, e.g., due to low signal-to-noise ratios (<3) in either the stellar surface density maps or the kinematic maps.

1. The observed deprojected angular momentum $J_i = \mathbf{r}_i \mathbf{v}_i m_i$ in every spaxel, i, at a deprojected radius, $\mathbf{r}$, whose circular velocity, $\mathbf{v}$, is derived from kinematic maps and a mass, m, from stellar surface density maps. The deprojection is based on the inclination and the position angle derived from a fit to the stellar surface density maps; the inclination and position angle are assumed to be constant with the radius. Noncircular motions are neglected in this work, but see S. M. Sweet et al. (2018, in preparation) for a treatment of the contribution of noncircular motions to total and spatially resolved j_*.

2. The model J_i at each spaxel is computed by fitting an exponential profile to the disk, in order to reach the total angular momentum, traced by the flat part of the rotation curve. The surface mass density is characterized by $\Sigma(\mathbf{r}_i) \propto \exp(-\mathbf{x}_i)$, where $\mathbf{x}_i = \mathbf{r}_i / r_{\text{flat}}$, and the exponential scale length, r_{flat}, is assumed to be the radius at which the velocity reaches the converged velocity v_{flat}. While not the case in general, this simplifying assumption is made in order to keep the number of free parameters at a minimum. The exponential fit is given by Equation (7) of OG14; $\bar{\mathbf{v}}_i \approx v_{\text{flat}}(1 - \exp(-\mathbf{x}_i))$. Following OG14's Equation (8), the model $J_i = 2((1 + \mathbf{x}_i)^3 - 1)/(1 + \mathbf{x}_i)^3 \mathbf{r}_i v_{\text{flat}} m_i$. The model is, on average, consistent with

the observed J to the 5% level, if both are summed over the same high signal-to-noise spaxels. However, note that the purpose of the model is only to serve as an estimate of J_i in the low signal-to-noise spaxels.

3. The total j_* is then given by J/M_*, where $J = |\sum^i J_i|$ is the norm of the sum over the observed J_i (where defined) and estimated J_i in other spaxels, integrated to $r_i = \infty$. Including the estimated J_i in the spaxels where data is missing comprises an average of 20% of the total j_*.

The uncertainty in this method is typically $\Delta j_*/j_* = \pm$ 5%–10%, which is predominantly contributed by the uncertainty in extrapolating $j_*(r)$ beyond where it is converged (that is, the assumption that the observations reach the flat part of the rotation curve), as well as the assumption of pure circular motion and the uncertainty in inclination (see OG14 for further details).

2.3. THINGS

THINGS (Walter et al. 2008) is a survey of 34 nearby galaxies observed to high multiples of the effective radius, r_e. OG14 presented j_* measured with H I kinematics for the 16 spiral THINGS galaxies that have stellar surface density maps published by Leroy et al. (2008). Stellar masses and uncertainty $\Delta M_*/M_* = \pm 0.11$ dex are also taken from OG14. This sample contains 13 galaxies with pseudobulges and 3 with classical bulges, with bulge-to-total mass ratios of $0 \leqslant \beta \leqslant 0.41$.

2.4. Romanowsky & Fall

RF12 presented j_* for a sample of spiral and elliptical galaxies, calculated using stellar kinematics from the slit spectroscopy of starlight and ionized gas. OG14 found these to vary systematically with respect to their own IFS observations, so we rescale RF12 j_* using Equation (6) of OG14:

$$\left(\frac{j_*}{10^3 \text{ kpc km s}^{-1}}\right) \approx 1.01 \left(\frac{\widetilde{j_*}}{10^3 \text{ kpc km s}^{-1}}\right)^{1.3}. \quad (1)$$

The relative uncertainty is $\Delta j_*/j_* = \pm 32\%$, given by the quadrature sum of the uncertainty in RF12 j_* (10%) and the rms scatter of the calibrating relation (30%).

RF12 derived M_* using Bell et al. (2003) colors and a diet Salpeter initial mass function (IMF) located between Kroupa (2001) and Salpeter (1955), which translates to an assumed K-band mass-to-light ratio of $M/L_K = 1\,M_\odot/L_{\odot,K}$. This differs from Leroy et al. (2008), who assumed a Kroupa (2001) IMF and consequently $M/L_K = 0.5\,M_\odot/L_{\odot,K}$. We therefore scale the RF12 M_* by 0.5 to achieve consistency with our THINGS sample. The uncertainty in RF12's M_* of $\Delta M_*/M_* = \pm 0.2$ dex is taken from OG14.

Motivated by the desire to calculate β and to classify the bulge type in the same manner as for our THINGS sample, we select the 25 galaxies from RF12 for which we have existing high-quality bulge–disk decompositions. The RF12 sample thus contains 12 galaxies that contain pseudobulges, 12 that contain classical bulges, and 1 whose bulge is unclassifiable (NGC 3593), with $0 \leqslant \beta \leqslant 0.53$.

2.5. CALIFA

The CALIFA survey made stellar kinematic and surface density maps available for 300 nearby galaxies (Falcón-Barroso et al. 2017). We use the OG14 method described above to measure j_* for these galaxies, and note that $j_*(<r)$ converges to $>0.99\,j_*$ at a radius of $r \sim 3\,r_e$. This motivates us to select the subset observed to at least that radius.

We take stellar masses from Falcón-Barroso et al. (2017), who used the methods outlined in Walcher et al. (2014); namely, we assume Bruzual & Charlot (2003) stellar populations and a Chabrier (2003) IMF. The rms scatter between their two implementations gives the uncertainty $\Delta M_*/M_* = \pm 0.15$ dex. The Bruzual & Charlot (2003) stellar populations were shown by Sánchez et al. (2013) to give stellar masses that are consistent with those derived from Bell & de Jong (2001) colors (which themselves are consistent with Bell et al. 2003, as used by Leroy et al. 2008). K-band M/L_K ratios based on the Chabrier (2003) IMF differ from those assuming a Kroupa (2001) IMF (as in Leroy et al. 2008) by only 10% (Longhetti & Saracco 2009, Table 2), which is well within the scatter. Hence, we are comfortable that the CALIFA stellar masses are comparable with those of our THINGS sample.

Hubble types are taken from Falcón-Barroso et al. (2017) and β from the bulge–disk decompositions presented in Méndez-Abreu et al. (2017). Méndez-Abreu et al. (2017) include only one FD08 galaxy: $\beta_{\text{FD08}} = 0.5$ cf. $\beta_{\text{CALIFA}} = 0.6$. Since the Méndez-Abreu et al. (2017) decompositions were based on Sloan Digital Sky Survey (SDSS) imaging, we estimate the uncertainty as $\Delta \beta_{\text{CALIFA}} = \pm 0.1$. We remove five pure elliptical galaxies, since j_*, as measured here, is strictly applicable to systems that contain a disk. There is a lack of imaging of sufficient resolution to reliably recover the bulge Sérsic index, so we do not categorize CALIFA galaxies into those with classical or pseudobulges. Our high-quality CALIFA subset comprises 35 spiral and 15 elliptical/lenticular galaxies and spans $0 \leqslant \beta \leqslant 0.73$.

The properties of the resulting samples are given in Table 1.

3. The Relation between Stellar Mass, Specific Angular Momentum, and Morphology

We present our M_*–j_*–β relation for THINGS, RF12, and CALIFA, fitting the data with the log-linear three-parameter model given in Equation (9) of OG14:

$$\beta = p_1 \log_{10} M_* + p_2 \log_{10} j_* + p_3, \quad (2)$$

where β is the bulge-to-total stellar mass ratio, M_* is the stellar mass in units of $10^{10}\,M_\odot$, and j_* is the stellar specific angular momentum in units of $10^3\,\text{kpc km s}^{-1}$. The maximum likelihood solution is easily computed using the hyper.fit algorithm of Robotham & Obreschkow (2015). This yields $p_1 = 0.39 \pm 0.04$, $p_2 = -0.38 \pm 0.06$, and $p_3 = 0.06 \pm 0.02$ with an intrinsic scatter of a standard deviation of $\sigma = 0.07 \pm 0.02$.[4] The uncertainties are standard deviations, i.e., the square roots of the diagonal elements of the covariance matrix, approximated as the negative inverse Hessian matrix of the likelihood at its maximum (Laplace approximation). The parameters are in agreement with OG14, while the scatter is increased due to revised β.

---

[4] The intrinsic Gaussian scatter of Equation (2) is defined along the β-axis, but can be propagated to another set of axes appropriate to the chosen independent variable, with consistent results. For example, writing Equation (2) as $\log_{10}(j_*) = q_1 \log_{10}(M^*) + q_2 \beta + q_3$ gives an intrinsic scatter of $\sigma = 0.20 \pm 0.05$ in $\log(j_*)$ and parameters $q_1 = 1.03 \pm 0.11$, $q_2 = -2.66 \pm 0.41$, $q_3 = 0.17 \pm 0.07$, which propagate identically back to p.
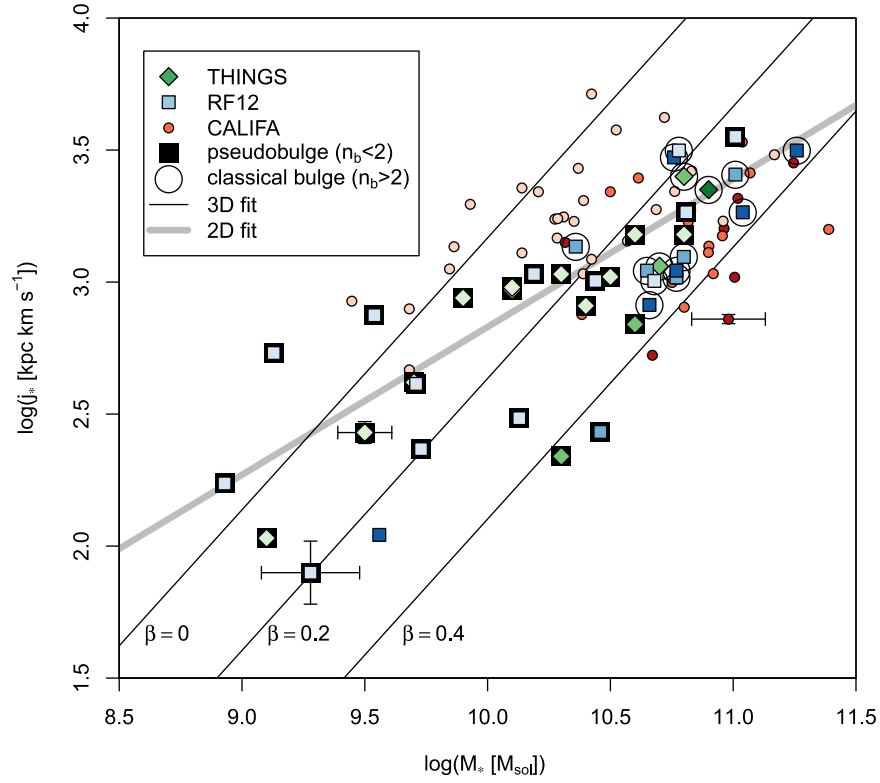
Figure 2. M_*–j_* plane. THINGS and RF12 symbols are the same as those in Figure 1, and CALIFA symbols are orange filled circles. Points are assigned discrete color shades according to bins of $\beta \in [0, 0.2, 0.4, 1]$. Black filled squares are placed around the galaxies that contain pseudobulges and unfilled circles around those that contain classical bulges, on the basis of the bulge Sérsic index. The bulge of NGC 3593 is not classifiable in this manner, so is unmarked, as are the CALIFA galaxies. A typical error bar is shown for each of the THINGS, RF12, and CALIFA subsamples. Lines of constant β represent a trivariate fit in M_*–j_*–β space (Equation (3)). The best-fitting exponent $\alpha = 1.03 \pm 0.11$ is consistent with $\alpha = 1$. The 2D fit (the thick gray line) gives $\alpha = 0.56 \pm 0.06$, consistent with CDM predictions for halos.

Table 1
Properties of Galaxies Presented in This Paper

Name	Survey	Type	M_* [log($M_\odot$)]	$\Delta M_*/M_*$ (dex)	β	$\Delta\beta$	r_d (kpc)	$r_{\rm flat}$ (kpc)	$v_{\rm flat}$ (km s^{-1})	j_* (kpc km s^{-1})	Δj_* (kpc km s^{-1})	$n_{\rm bulge}$
(1)	(2)	(3)	(4)	(5)	(6)	(7)	(8)	(9)	(10)	(11)	(12)	(13)
NGC 0628	THINGS	Sc	10.10	0.11	0.17	0.05	2.3	0.8	217	955	95	1.53
NGC 0925	THINGS	SBcd	9.90	0.11	0.06	0.05	4.1	6.5	136	871	87	0.90
NGC 2403	THINGS	SBc	9.70	0.11	0.06	0.05	1.6	1.7	134	417	42	0.80
...	...	...	...	...	...	...	...	...	...	...	...	...
NGC 0224	RF12	Sb	10.76	0.20	0.48	0.05	5.9	...	234	2967	938	2.13
NGC 0247	RF12	Sd	9.54	0.20	0.00	0.05	4.1	...	92	749	237	0.00
NGC 0300	RF12	Sd	8.93	0.20	0.00	0.05	1.6	...	60	173	55	1.64
...	...	...	...	...	...	...	...	...	...	...	...	...
IC 1151	CALIFA	Scd	9.85	0.15	0.02	0.10	1.9	4.0	113	1122	154	...
MCG-02-02-030	CALIFA	Sb	10.37	0.15	0.08	0.10	3.1	8.8	177	2698	340	...
NGC 0001	CALIFA	Sbc	10.80	0.15	0.46	0.10	1.8	3.4	169	1564	117	...
...	...	...	...	...	...	...	...	...	...	...	...	...

Note. Columns: (1) galaxy identifier; (2) data set; (3) Hubble type; (4) log(stellar mass); (5) measurement uncertainty in M_*; (6) bulge-to-total ratio; (7) measurement uncertainty in β; (8) scale length; (9) radius at which rotation curve becomes flat; (10) asymptotic velocity; (11) stellar specific angular momentum; (12) measurement uncertainty in j_*; and (13) bulge Sérsic index.

(This table is available in its entirety in machine-readable form.)

In Figure 2 we show the M_*–j_* projection, overlaid with lines of constant β. These best-fitting lines take the form of Equation (10) of OG14:

$$\frac{j_*}{10^3 \text{ kpc km s}^{-1}} = k e^{(-g\beta)} \left(\frac{M_*}{10^{10} M_\odot} \right)^\alpha, \qquad (3)$$

where coefficients k and g together are instructed by baryonic physics, g modifies the bulge-dependent scale, and the exponent α is predicted by CDM to be $\alpha = 2/3$ for DM halos. Equation (3) is simply obtained by potentiating Equation (2). Since our observational uncertainties tend to be normal in log(M_*), log(j_*), and β (with the exception that $0 \leqslant \beta \leqslant 1$),

Table 2
Coefficients for Best-fitting Lines

M_*–j_* Relation (Equation (3))	k	g	α
This work:			
All	1.47 ± 0.24	6.13 ± 0.95	1.03 ± 0.11
THINGS	1.38 ± 0.52	8.65 ± 3.07	1.27 ± 0.27
RF12	1.75 ± 0.82	6.60 ± 2.31	1.07 ± 0.21
CALIFA	1.76 ± 0.25	4.25 ± 0.79	0.63 ± 0.12
Pseudobulge ($n_b < 2$)	1.21 ± 0.30	6.94 ± 1.82	0.86 ± 0.12
OG14:			
Fixed α	0.91 ± 0.09	7.59 ± 0.79	1.00
Free α	0.89 ± 0.11	7.03 ± 1.35	0.94 ± 0.07
β–j_*/M_* Relation (Equation (4))	k_1	k_2	
This work:			
All	-0.35 ± 0.04	0.08 ± 0.02	
Pseudobulge, all	-0.26 ± 0.06	0.05 ± 0.03	
Pseudobulge, THINGS	-0.23 ± 0.06	0.04 ± 0.02	
OG14	-0.30 ± 0.03	-0.01 ± 0.01	

Note. Coefficients of best-fitting lines for Equations (3) and (4).

rather than in M_*, j_*, and $\exp(\beta)$, it is sensible to fit the parameters $p = \{p_1, p_2, p_3\}$ of Equation (2) and to propagate them to the parameters $q = \{k = 10^{(-p_3/p_2)}, g = -\ln(10)/p_2, \alpha = -p_1/p_2\}$ of Equation (3). The covariance matrix, C_q, of the new parameters, q, can then be estimated by linearly propagating the covariance matrix, C_p, of the parameters, p, i.e., $C_q = JC_pJ^\dagger$, where the Jacobian J is defined as $J_{ij} = \partial q_i/\partial p_j$. This method is consistent with the fitting of Equation (3), assuming log-normal uncertainties in M_* and j_* and normal in β. Note that the orthogonal scatter does not fit here and is also minimized (see Robotham & Obreschkow 2015 for details).

We give the resulting coefficients and their uncertainties in Table 2. We find $\alpha = 1.03 \pm 0.11$, consistent with OG14. The importance of correctly accounting for measurement uncertainties in all variables, as well as an intrinsic scatter, is demonstrated by the fact that a simple, linear least-squares fit to Equation (3), which only accounts for measurement uncertainties in j_* and not the intrinsic scatter, yields a significantly different exponent, $\alpha = 0.66 \pm 0.06$. The bulge dependence g and prefactor k from our fit to Equation (2) are also consistent with OG14 at the 3-σ level. The fits for THINGS or RF12 alone are consistent with the main sample; CALIFA is significantly different, but this is likely due to their angular size selection function, which results in a lack of low-mass, low-j_* galaxies. Galaxies certain to contain a pseudobulge (or no bulge) are consistent with the main sample. Conversely, the galaxies in our sample that contain classical bulges do not have sufficient dynamic ranges in M_* to measure the presence or absence of a relation.

The corresponding two-dimensional fit to $j_* \propto M_*^\alpha$ (that is, ignoring the effect of β) can be found in a similar manner by fitting $\log j_* = \alpha \log(M_*) + a$; this gives $\alpha = 0.56 \pm 0.06$, consistent with the CDM prediction for halos of $\alpha = 2/3$.

In Figure 3 we fix $\alpha = 1$ and show the β–j_*/M_* relation for pseudobulges and for all bulge types. The best-fitting lines take

the form of Equation (11) of OG14:

$$\beta = k_1 \log\left(\frac{j_* M_*^{-1}}{10^{-7}\ \text{kpc km s}^{-1}\ M_\odot^{-1}}\right) + k_2, \qquad (4)$$

with coefficients k_1 and k_2 given in Table 2. This is obtained by imposing $p_2 = -p_1$ in Equation (2) and propagating parameters $p = \{p_1, -p_1, p_3\}$ to $q = \{k_1 = -p_1, k_2 = p_3, \alpha = -p_1/p_2 = 1\}$. The fit to all bulge types has a slope of $k_1 = -0.35 \pm 0.04$. Galaxies with high $\beta \gtrsim 0.4$ (where most are dominated by a classical bulge) all lie above this relation, indicating a high β for their j_* and stellar mass. The sample of galaxies that host pseudobulges follows a shallower relation to the fit to galaxies with all bulge types, with $k_1 = -0.26 \pm 0.06$, exhibiting a lower β for a given j_*/M_* than those that contain classical bulges. Galaxies that contain classical bulges have a small range of M_*, so we cannot determine whether or not there is a corresponding relation for that sample. Our sample of THINGS galaxies with pseudobulges is marginally consistent with and follows a shallower relation than OG14 (which is predominantly composed of galaxies that host pseudobulges); the main difference is a direct result of our revised β.

4. Discussion and Conclusion

In Section 3 we presented the relation between specific angular momentum, stellar mass, and bulge-to-total mass ratio. Galaxies with pseudobulges have lower β per j_*/M_* than those with classical bulges and exhibit a well-defined track in β–j_*/M_* space.

We investigate over what range in β the β–j_*/M_* relation applies. Figure 3 illustrates that the relation for all galaxies extends to $\beta \sim 0.4$, albeit with some scatter, partly arising from the difficulty in measuring β. As discussed in Section 2, we employ bulge–disk decompositions for the three data sets presented here. The methods for RF12 and OG14 are identical, but the CALIFA decompositions may subtly differ due to the different imaging and software used. There may be also systematic differences between samples owing to the type of kinematics used in this study: stellar for CALIFA and RF12, and H I for THINGS. First, we assume (as in OG14) that the H I and stars corotate, but asymmetric drift may be appreciable, contributing to j_gas being higher than j_* by 0.1 dex (Cortese et al. 2016). Those j_gas were measured from Hα kinematics, not H I, so we cannot apply the magnitude of that correction, but the direction of the effect will likewise be in the opposite direction of that required. Second, stellar kinematics trace both the disk and bulge, but H I kinematics trace only the disk. Inclusion of the bulge component in the THINGS measurements would serve to increase j_* toward the CALIFA and RF12 values, but only at an average of 0.3% and a maximum of 1.3% (OG14). Neither effect explains why many of the CALIFA and RF12 galaxies with $\beta \gtrsim 0.4$ lie significantly above the relation defined by all three samples. The apparent upturn may seem to suggest that the true relation takes a different functional form than that assumed here.

In general, mechanisms that increase bulge mass appear to decrease the ratio of j_*/M_*. The relation first presented in OG14 for $0 \leqslant \beta \leqslant 0.32$ is confirmed here for $0 \leqslant \beta \lesssim 0.4$, but breaks down for $\beta \gtrsim 0.4$. At fixed j_*/M_*, galaxies hosting a classical bulge exhibit a range of β, extending upward from
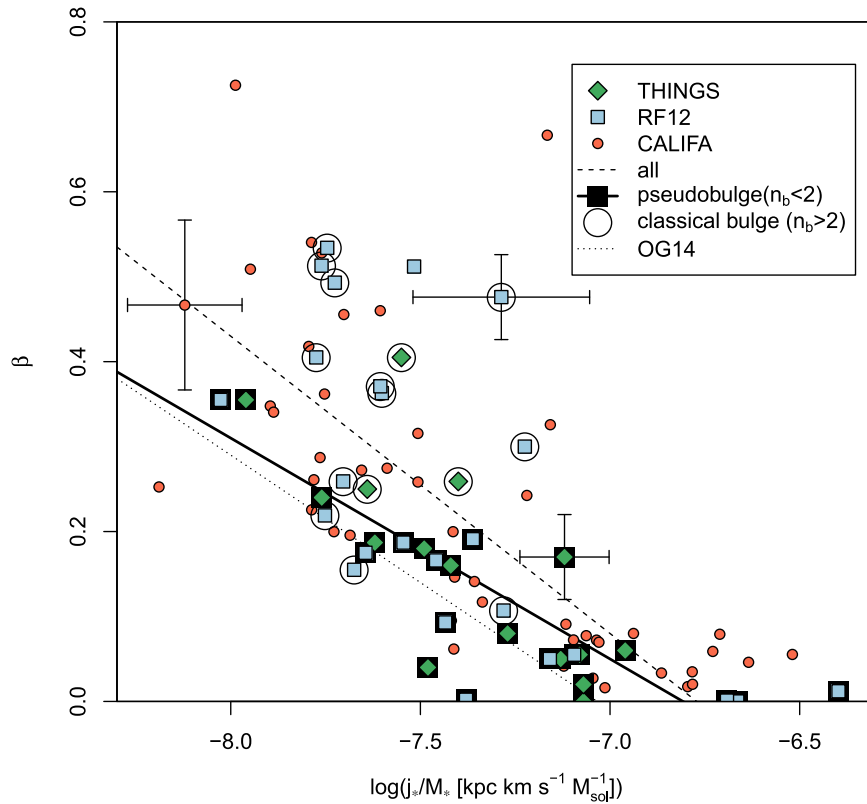
Figure 3. β–j_*/M_* relation. Symbols are the same as those for Figure 2. The solid line fits galaxies that contain a pseudobulge, the dashed line fits the entire sample, and the dotted line gives OG14. Pseudobulges appear to follow a separate sequence from classical bulges, consistent with a separate evolutionary track.

the relation defined by galaxies that host a pseudobulge. A large β for classical galaxies is well explained by noting that in Figure 2, galaxies that host classical bulges are generally more massive than those that contain pseudobulges (and see Fisher & Drory 2016) and that more massive galaxies typically have larger β (Koda et al. 2009). The same general trend is also seen in the Evolution and Assembly of GaLaxies and their Environments simulations (EAGLE, Schaye et al. 2015; Lagos et al. 2018), where the most bulge-dominated galaxies lie above the best-fitting line. This is interpreted as those galaxies having higher j_* than predicted by the relation, which points to an absence of gas-poor mergers (Lagos et al. 2018).

Interestingly, $j_* \propto M_*^\alpha$ is well fit by $\alpha = 1$ for fixed β over all bulge types, which is in line with the finding of OG14 for their sample of predominantly galaxies with small pseudo-bulges. OG14 outlined a theoretical argument for a physical motivation to an exponent $\alpha = 1$ for a given morphology, whereby j_*/M_* traces inverse surface density, which is inversely related to the Toomre (1964) Q parameter. Q quantifies instability against rotation, which is required for pseudobulge formation, so Q decreases while β increases. Testing this interpretation is outside of the scope of this paper but would make for an interesting future work.

When ignoring the β dimension, we find $\alpha \sim 2/3$, as seen by Fall (1983), OG14, and Cortese et al. (2016). This confirmation is notwithstanding several important distinctions, namely: a different bulge decomposition method from those of Fall (1983), OG14, and Cortese et al. (2016), the nonlinear correction applied to the Fall (1983) j_* to approximate our integral field unit data, the use of data out to $3r_e$ cf. $1r_e$ in Cortese et al. (2016), and the extended range of morphology with respect to OG14. This exponent is consistent with the

CDM prediction for halos, $j_h \propto M_h^{2/3}$. Connecting that prediction with our observed relation for stars implies that M_* and j_* depend, respectively, on M_h and j_h with the same functional form. The M_*–M_h relation is shown to be complex (Guo et al. 2010); future large IFS surveys (e.g., Hector, Lawrence et al. 2012) are required to test whether the j_*–j_h relation takes a similar form.

We investigate the possibility of two β–j_*/M_* tracks: one for galaxies with classical bulges, which is thought to be formed by merging; and the other for galaxies with pseudobulges, formed by secular evolution (Wyse et al. 1997; Kormendy & Kennicutt 2004). Secular evolution refers to angular momentum transport causing some disk material to fall toward the galaxy center, contributing to the pseudobulge with a small increase in β. The same process feeds star formation in the pseudobulge, which causes a small amount of j_* to be lost in outflows due to stellar winds. There is a corresponding small change in M_*, so the galaxy moves along a well-defined track in β–j_*/M_*. This is consistent with the distinct relation we find for pseudobulges. The lower β implies that the processes that form pseudobulges are less efficient at rearranging j_* and M_* while forming bulges than those responsible for classical bulges.

Conversely, mergers can significantly increase both M_* and j_*, though some j_* will be canceled due to the misalignment of the galaxy spin axes (Romanowsky & Fall 2012; Lagos et al. 2018). There is a correspondingly large increase in β, so mergers move a galaxy above the pseudobulge β–j_*/M_* relation, while forming a classical bulge. We cannot include EAGLE as a control sample in Figure 3, since the EAGLE β are measured from kinematic bulge–disk decompositions instead of photometric methods. As a result, they are expected

to be, on average, larger than our β by ~ 0.5 (Obreja et al. 2016). In addition to this systematic offset, there is considerable scatter, so one cannot apply a simple correction factor. In future work (C. Lagos et al. 2018, in preparation), we will present "photometric" bulge–disk decompositions of the synthetic images of galaxies to obtain β measurements that are directly comparable to observations. While EAGLE β are not directly comparable with our β, we can use those simulations to make quantitative predictions of the movement along the j_*/M_* axis, since mergers, which build classical bulges, appear to do so while moving the galaxy above the pseudobulge relation. We see in Figure 3 that galaxies that host classical bulges lie on or above the pseudobulge relation, so we use that relation to calculate a lower limit to $\Delta\beta$ for mergers that build classical bulges. Lagos et al. (2018) predict that a typical dry (wet) minor merger[5] that increases M_* by $\Delta M_* = 0.15$ dex will decrease (increase) j_* by $\Delta j_* = -0.15(0.04)$ dex. Combining the EAGLE predictions with our observed relation for galaxies that contain pseudobulges, we expect that minor mergers of $\Delta M_* = 0.15$ dex will increase β by more than $\Delta\beta \geqslant 0.08(0.03)$. Assuming that a bulgeless progenitor of a galaxy with a classical bulge begins at $\log(j_*/M_*) \sim -6.75$, then several mergers of this magnitude would be required to achieve $-7.7 \lesssim \log(j_*/M_*) \lesssim -7.2$, as we observe. Alternatively, a galaxy that already hosts a pseudobulge and lies in that j_*/M_* range may only need to experience one such merger to form a classical bulge with those properties. However, it is not known where the progenitors of classical bulge galaxies lie in β–j_*/M_* space. In reality there is a range of possible merger ratios, which increases the range of expected $\Delta\beta$, and may serve to explain the observed dispersion in β–j_*/M_*. The apparent failure of the relation for high β may then simply reflect the difference between the pseudobulge and classical bulge regimes. We note that other physical processes, such as outflows, also modify j_*; these will be discussed further in S. M. Sweet et al. (2018, in preparation), when we present the internal distribution of j_*.

The dependence on the bulge type that we see in the β–j_*/M_* relation is reminiscent of the black hole mass—galaxy velocity dispersion $M_{\rm BH}$–σ relation (Ferrarese & Merritt 2000; Gebhardt et al. 2000), where galaxies with classical bulges follow a well-defined relation in $M_{\rm BH}$–σ space, but those that contain pseudobulges show no such relation, as suggested by Kormendy & Gebhardt (2001) and shown by Hu (2008) and Saglia et al. (2016). In this paper we see the opposite effect for β–j_*/M_*, where it is instead galaxies with pseudobulges that show the well-defined relation, and those with classical bulges that do not. This is consistent with earlier suggestions that classical bulges are sensitive to black hole evolution, while the evolution of pseudobulges is linked to the disk, which dominates the j_* budget (Kormendy & Ho 2013).

In conclusion, we have presented high-quality integrated specific angular momenta for a subset of CALIFA galaxies and revisited the stellar mass—specific angular momentum—morphology relation for $0 \leqslant \beta \leqslant 0.73$, using galaxies from THINGS, RF12, and CALIFA. We confirm the OG14 β–j_*/M_* relation for galaxies that host pseudobulges, albeit with an increased scatter. The relation does not describe galaxies with classical bulges, which is in line with separate evolutionary channels for the formation of the two major bulge

types. Future work will employ a large, homogeneous sample with high-quality measurements of β and j_* to mitigate selection biases and to confirm the strength of this relation. The next critical stage is to understand the place of progenitors of galaxies that contain classical bulges, with a detailed study of specific angular momentum in main-sequence, high-redshift galaxies.

ORCID iDs

Sarah M. Sweet https://orcid.org/0000-0002-1576-2505
Karl Glazebrook https://orcid.org/0000-0002-3254-9044
Danail Obreschkow https://orcid.org/0000-0002-1527-0762
Claudia Lagos https://orcid.org/0000-0003-3021-8564

References

Agertz, O., Teyssier, R., & Moore, B. 2011, MNRAS, 410, 1391
Allen, J. T., Croom, S. M., Konstantopoulos, I. S., et al. 2015, MNRAS, 446, 1567
Barnes, J., & Efstathiou, G. 1987, ApJ, 319, 575
Bassett, R., Bekki, K., Cortese, L., & Couch, W. 2017, MNRAS, 471, 1892
Bell, E. F., & de Jong, R. S. 2001, ApJ, 550, 212
Bell, E. F., McIntosh, D. H., Katz, N., & Weinberg, M. D. 2003, ApJS, 149, 289

---

[5] Mass ratio <1:3.

Bertola, F., Cinzano, P., Corsini, E. M., et al. 1996, ApJL, 458, L67
Bruzual, G., & Charlot, S. 2003, MNRAS, 344, 1000
Bryant, J. J., Owers, M. S., Robotham, A. S. G., et al. 2015, MNRAS, 447, 2857
Catelan, P., & Theuns, T. 1996a, MNRAS, 282, 436
Catelan, P., & Theuns, T. 1996b, MNRAS, 282, 455
Chabrier, G. 2003, PASP, 115, 763
Cortese, L., Fogarty, L. M. R., Bekki, K., et al. 2016, MNRAS, 463, 170
Croom, S. M., Lawrence, J. S., Bland-Hawthorn, J., et al. 2012, MNRAS, 421, 872
Fabricius, M. H., Saglia, R. P., Fisher, D. B., et al. 2012, ApJ, 754, 67
Falcón-Barroso, J., Lyubenova, M., van de Ven, G., et al. 2017, A&A, 597, A48
Fall, S. M. 1983, in IAU Symp. 100, Internal Kinematics and Dynamics of Galaxies, ed. E. Athanassoula (Dordrecht: Reidel Publishing), 391
Ferrarese, L., & Merritt, D. 2000, ApJL, 539, L9
Fisher, D. B., Bolatto, A., Drory, N., et al. 2013, ApJ, 764, 174
Fisher, D. B., & Drory, N. 2008, AJ, 136, 773
Fisher, D. B., & Drory, N. 2010, ApJ, 716, 942
Fisher, D. B., & Drory, N. 2011, ApJL, 733, L47
Fisher, D. B., & Drory, N. 2016, in Galactic Bulges, Vol. 418, ed. E. Laurikainen, R. Peletier, & D. Gadotti (Cham: Springer), 41
Gebhardt, K., Bender, R., Bower, G., et al. 2000, ApJL, 539, L13
Governato, F., Brook, C., Mayer, L., et al. 2010, Natur, 463, 203
Guo, Q., White, S., Li, C., & Boylan-Kolchin, M. 2010, MNRAS, 404, 1111
Hernandez, X., & Cervantes-Sodi, B. 2006, MNRAS, 368, 351
Hu, J. 2008, MNRAS, 386, 2242
Husemann, B., Jahnke, K., Sánchez, S. F., et al. 2013, A&A, 549, A87
Kent, S. M. 1986, AJ, 91, 1301
Koda, J., Milosavljević, M., & Shapiro, P. R. 2009, ApJ, 696, 254
Kormendy, J., & Gebhardt, K. 2001, in AIP Conf. Ser. 586, 20th Texas Symposium on Relativistic Astrophysics, ed. J. C. Wheeler & H. Martel (Melville, NY: AIP), 363
Kormendy, J., & Ho, L. C. 2013, ARA&A, 51, 511
Kormendy, J., & Kennicutt, R. C., Jr. 2004, ARA&A, 42, 603
Kroupa, P. 2001, MNRAS, 322, 231
Lagos, C. d. P., Stevens, A. R. H., Bower, R. G., et al. 2018, MNRAS, 473, 4956
Lawrence, J., Bland-Hawthorn, J., Bryant, J., et al. 2012, Proc. SPIE, 8446, 844653
Leroy, A. K., Walter, F., Brinks, E., et al. 2008, AJ, 136, 2782
Longhetti, M., & Saracco, P. 2009, MNRAS, 394, 774
Méndez-Abreu, J., Ruiz-Lara, T., Sánchez-Menguiano, L., et al. 2017, A&A, 598, A32
Mo, H. J., Mao, S., & White, S. D. M. 1998, MNRAS, 295, 319
Obreja, A., Stinson, G. S., Dutton, A. A., et al. 2016, MNRAS, 459, 467
Obreschkow, D., & Glazebrook, K. 2014, ApJ, 784, 26
Obreschkow, D., Glazebrook, K., Bassett, R., et al. 2015, ApJ, 815, 97
Ravindranath, S., Ho, L. C., Peng, C. Y., Filippenko, A. V., & Sargent, W. L. W. 2001, AJ, 122, 653
Robotham, A. S. G., & Obreschkow, D. 2015, PASA, 32, e033
Romanowsky, A. J., & Fall, S. M. 2012, ApJS, 203, 17
Saglia, R. P., Opitsch, M., Erwin, P., et al. 2016, ApJ, 818, 47
Salpeter, E. E. 1955, ApJ, 121, 161
Sánchez, S. F., García-Benito, R., Zibetti, S., et al. 2016, A&A, 594, A36
Sánchez, S. F., Kennicutt, R. C., Gil de Paz, A., et al. 2012, A&A, 538, A8
Sánchez, S. F., Rosales-Ortega, F. F., Jungwiert, B., et al. 2013, A&A, 554, A58
Sandage, A., & Bedke, J. 1994, The Carnegie Atlas of Galaxies, Vol. I and II (Washington, DC: Carnegie Inst. for Science Publishing)
Schaye, J., Crain, R. A., Bower, R. G., et al. 2015, MNRAS, 446, 521
Schweizer, F. 1990, in Proc. Int. Conf. on Dynamics and Interactions of Galaxies, ed. R. Wielen (New York: Springer), 60
Sérsic, J. L. 1963, BAAA, 6, 41
Sharp, R., Allen, J. T., Fogarty, L. M. R., et al. 2015, MNRAS, 446, 1551
Sweet, S. M., Drinkwater, M. J., Meurer, G., et al. 2016, MNRAS, 455, 2508
Toomre, A. 1964, ApJ, 139, 1217
Toomre, A. 1977, in Evolution of Galaxies and Stellar Populations, ed. B. M. Tinsley, R. B. G. Larson, & D. Campbell (New Haven, CT: Yale Univ. Press), 401
van den Bosch, F. C., Burkert, A., & Swaters, R. A. 2001, MNRAS, 326, 1205
Walcher, C. J., Wisotzki, L., Bekeraité, S., et al. 2014, A&A, 569, A1
Walter, F., Brinks, E., de Blok, W. J. G., et al. 2008, AJ, 136, 2563
Wyse, R. F. G., Gilmore, G., & Franx, M. 1997, ARA&A, 35, 637